Global quark polarization in noncentral $A+A$ collisions

Jian-Hua Gao,[1] Shou-Wan Chen,[2] Wei-tian Deng,[1,3] Zuo-Tang Liang,[1] Qun Wang,[2] and Xin-Nian Wang[1,3]
[1]*Department of Physics, Shandong University, Jinan, Shandong 250100, People's Republic of China*
[2]*Department of Modern Physics, University of Science and Technology of China, Hefei, Anhui 230026, People's Republic of China*
[3]*Nuclear Science Division, MS 70R0319, Lawrence Berkeley National Laboratory, Berkeley, California 94720, USA*
(Received 12 October 2007; revised manuscript received 28 December 2007; published 9 April 2008)

Partons produced in the early stage of noncentral heavy-ion collisions can develop a longitudinal fluid shear because of the unequal local number densities of participant target and projectile nucleons. Under such fluid shear, local parton pairs with nonvanishing impact parameters have finite local relative orbital angular momentum along the direction opposite to the reaction plane. Such a finite relative orbital angular momentum among locally interacting quark pairs can lead to global quark polarization along the same direction because of spin-orbital coupling. Local longitudinal fluid shear is estimated within both the Landau fireball and the Bjorken scaling model of initial parton production. Quark polarization through quark-quark scatterings with the exchange of a thermal gluon is calculated beyond the small-angle scattering approximation in a quark-gluon plasma. The polarization is shown to have a nonmonotonic dependence on the local relative orbital angular momentum dictated by the interplay between electric and magnetic interactions. It peaks at a value of relative orbital angular momentum which scales with the magnetic mass of the exchanged gluons. With the estimated small longitudinal fluid shear in semiperipheral Au+Au collisions at energies currently available at the BNL Relativistic Heavy Ion Collider (RHIC), the final quark polarization is found to be small $|P_q| < 0.04$ in the weak coupling limit. Possible behavior of the quark polarization in the strong coupling limit and implications on the experimental detection of such global quark polarization at RHIC and CERN Large Hadron Collider (LHC) are also discussed.

DOI: 10.1103/PhysRevC.77.044902 PACS number(s): 25.75.−q, 13.88.+e, 12.38.Mh

I. INTRODUCTION

Collective phenomena and jet quenching as observed in high-energy heavy-ion collisions at the BNL Relativistic Heavy Ion Collider (RHIC) provide strong evidence for the formation of a strongly coupled quark-gluon plasma [1,2]. Elliptic flow or azimuthal anisotropy of the hadron spectra in semiperipheral heavy-ion collisions and its agreement with the ideal hydrodynamic calculations [3] indicate a near perfect fluid behavior of the produced dense matter. Such an empirical observation of small shear viscosity [4] is consistent with the large value of the jet transport parameter as extracted from the jet quenching study of both single and dihadron spectra suppression [5]. Study of the collective behavior is made possible by investigating hadron spectra in the central rapidity region in noncentral or semiperipheral heavy-ion collisions. Extending the study to the large rapidity region of noncentral heavy-ion collisions should provide more information about not only the initial condition for the formation of the dense matter [6] but also the dynamical properties of the strongly coupled quark-gluon plasma.

Considering the longitudinal momentum distribution at various transverse positions in a noncentral heavy-ion collision, one will find a longitudinal fluid shear distribution representing local relative orbital angular momentum. Recently, it has been pointed out that the presence of such a local orbital angular momentum of the partonic system at the early stage of noncentral heavy-ion collisions can lead to a global polarization of quarks and antiquarks [7] in the direction orthogonal to the reaction plane. Understanding the spin-orbital interaction inside a strongly coupled system can open a new window to the properties of quark-gluon plasma (QGP). Although no detailed calculations have been carried out, an estimate using a screened static potential model in the small-angle approximation shows qualitatively that spin-orbital coupling in quantum chromodynamics (QCD) can lead to a finite global quark and antiquark polarization. Such a global quark/antiquark polarization should have many observable consequences such as global hyperon polarization [7,8] and vector meson spin alignment [9]. Predictions have been made [7,9] for these measurable quantities as functions of the global quark polarization P_q in various hadronization scenarios. Since the reaction plane in heavy-ion collisions can be determined in experiments by measuring the elliptic and direct flows, measurements of the global hyperon polarization or vector meson spin alignment become feasible. These measurements at RHIC are being carried out, and some of the preliminary results have already been reported [10–16].

The estimate of the global quark polarization in Ref. [7] was obtained by evaluating the polarization cross section in the impact parameter space with a small-angle approximation in an effective potential model. The analytical result

$$P_q = -\pi\mu p/2E(E+m_q) \tag{1}$$

has an intuitive expression, where p is the average c.m. momentum of two partons with an average transverse separation $1/\mu$ due to the longitudinal fluid shear. However, for a massless quark in a small longitudinal fluid shear, the obtained quark polarization P_q can become larger than unity, indicating the breakdown of the small-angle approximation. A more realistic estimate in noncentral heavy-ion collisions at RHIC indicates a small value of the average longitudinal fluid shear. Therefore, it is imperative to have a more realistic estimate of the quark

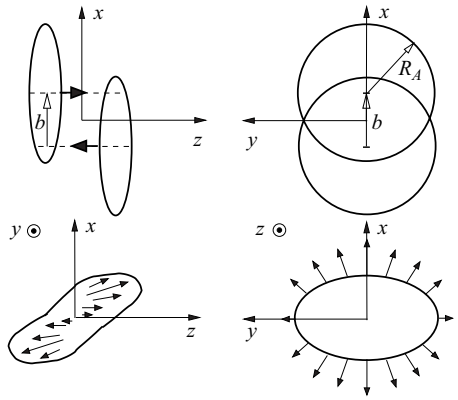

FIG. 1. Noncentral heavy-ion collision with impact parameter $\vec{b}$. The global angular momentum of the produced dense matter is along $-\hat{y}$, opposite to the reaction plane.

polarization P_q beyond the small-angle approximation. This will be the focus of this paper.

The rest of the paper is organized as follows. In Sec. II, we calculate the average longitudinal fluid shear in two different models of parton production. In a Landau fireball picture, a wounded nucleon model of bulk parton production in heavy-ion collisions is used with both simple hard-sphere and more realistic Wood-Saxon nuclear geometry. In the Bjorken scaling scenario, we use HIJING Monte Carlo model to estimate the transverse shear of the rapidity distribution of the produced parton in heavy-ion collisions at the RHIC energy which will be used to estimate the longitudinal fluid shear in the local comoving frame of the plasma. In Sec. III, we use the hard thermal loop (HTL) resummed gluon propagator in the comoving frame of the local longitudinal fluid cell to extend the calculation of quark polarization in Ref. [7] beyond the small-angle approximation and discuss the relative contributions from the electric and magnetic parts of quark-quark scattering. Finally in Sec. IV, we discuss the numerical results and their implications for experimental measurements at RHIC.

II. ORBITAL ANGULAR MOMENTUM AND SHEAR FLOW

Let us consider two colliding nuclei with the projectile of beam momentum per nucleon $\vec{p}_{\rm in}$ moving in the direction of the z axis, as illustrated in Fig. 1. The impact parameter $\vec{b}$, defined as the transverse distance of the center of the projectile nucleus from that of the target, is taken to be along the $\hat{x}$ direction. The normal direction $\vec{n}_b$ of the reaction plane, given by

$$\vec{n}_b \equiv \frac{\vec{p}_{\rm in}\times\vec{b}}{|\vec{p}_{\rm in}\times\vec{b}|}, \tag{2}$$

is along $\hat{y}$. For a noncentral collision, the two colliding nuclei carry a finite global orbital angular momentum L_y along the direction orthogonal to the reaction plane $(-\hat{y})$. How such a global orbital angular momentum is transferred to the final state particles depends on the equation of state (EOS) of the dense matter. At low energies, the final state is expected to be the normal nuclear matter with an EOS of rigid nuclei. A rotating compound nucleus can be formed when the colliding energy is comparable to or smaller than the nuclear binding energy. The finite value of the total orbital angular momentum of the noncentral collision at such low energies provides a useful tool for the study of the properties of superdeformed nuclei under such rotation [17]. At high colliding energy at RHIC, the dense matter is expected to be partonic with an EOS of the quark-gluon plasma. Given such a soft EOS, the global orbital angular momentum would probably never lead to the global rotation of the dense matter. Instead, the total angular momentum will be distributed across the overlapped region of nuclear scattering and is manifested in the shear of the longitudinal flow leading to a finite value of local vorticity density. Under such longitudinal fluid shear, a pair of scattering partons will on average carry a finite value of relative orbital angular momentum in the direction opposite to the reaction plane as defined in Eq. (2). According to Ref. [7], quark (or antiquark) will acquire a global polarization after such scatterings through the spin-orbital coupling in QCD.

The magnitude of the total orbital angular momentum L_y and the resulting longitudinal fluid shear can both be estimated within the wounded nucleon model of particle production in which the number of produced particles is assumed to be proportional to the number of participant nucleons. The transverse distributions (integrated over y) of participant nucleons in each nucleus can be written as

$$\frac{dN^{P,T}_{\rm part}}{dx} = \int dy\, dz \rho^{P,T}_A(x,y,z,b), \tag{3}$$

in terms of the participant nucleon number density $\rho^{P,T}_A(x,y,z,b)$ in nucleus A in the coordinate system defined above. The superscript P or T denotes projectile or target, respectively. The total orbital angular momentum L_y of the two colliding nuclei can be defined as

$$L_y = -p_{\rm in}\int x dx\left(\frac{dN^P_{\rm part}}{dx} - \frac{dN^T_{\rm part}}{dx}\right), \tag{4}$$

where $p_{\rm in}$ is the momentum per incident nucleon.

We assume the Woods-Saxon nuclear distribution

$$f^{P,T}_{\rm WS}(x,y,z,b) = C\left(1+\exp\frac{\sqrt{(x\mp b/2)^2+y^2+z^2}-R_A}{a}\right)^{-1}. \tag{5}$$

The participant nucleon number density is then

$$\rho^{P,T}_{A,WS}(x,y,z,b) = f^{P,T}_{\rm WS}(x,y,z,b)\left\{1-\exp\left[-\sigma_{NN}\times\int dz f^{T,P}_{\rm WS}(x,y,z,b)\right]\right\}, \tag{6}$$

where $\sigma_{NN}\approx 42$ mb is the total cross section of nucleon-nucleon scatterings at the RHIC energy, C is the normalization constant, and a is the width parameter set to $a = 0.54$ fm.

Shown in Fig. 2 as the solid line is the numerical value of L_y as a function of b for the Woods-Saxon nuclear distribution. As a comparison, we also plot as the dashed line the L_y distribution with a hard-sphere nuclear distribution which was

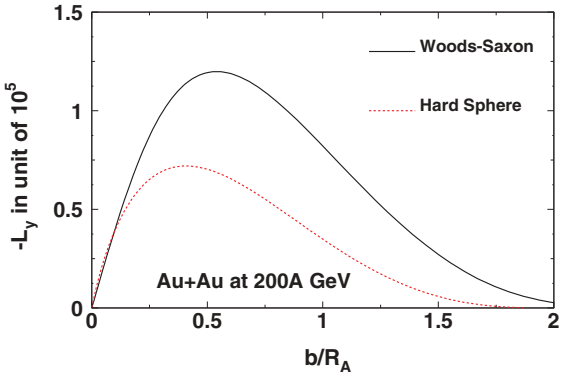

FIG. 2. (Color online) Total orbital angular momentum of the overlapping system in Au+Au collisions at the RHIC energy as a function of the impact parameter b.

used in Ref. [7]. With the hard-sphere nuclear distribution, the participant nucleon density is given by the overlapping area of two hard spheres, that is,

$$\rho^{P,T}_{A,\mathrm{HS}}(x,y,z,b) = f^{P,T}_{A,\mathrm{HS}}(x,y,z,b) \times \theta\big(R_A - \sqrt{(x \pm b/2)^2 + y^2 + z^2}\big), \quad (7)$$

and

$$f^{P,T}_{A,\mathrm{HS}}(x,y,z,b) = \frac{3A}{4\pi R_A^3}\theta\big(R_A - \sqrt{(x \mp b/2)^2 + y^2 + z^2}\big), \quad (8)$$

where $R_A = 1.12A^{1/3}$ is the nuclear radius and A the atomic number. We note significant differences between the two nuclear geometries in the total orbital angular momentum L_y in the overlapped region of two colliding nuclei. In both cases, the total orbital angular momentum is huge and of the order of 10^4 at most impact parameters.

Since RHIC data indicate the formation of a strongly coupled quark-gluon plasma [1], we can assume that a partonic system is formed immediately following the initial collision, and interactions among partons will lead to both transverse (in the x-y plane) and longitudinal collective motion in the QGP. The total orbital angular momentum carried by the produced system will manifest in the longitudinal flow shear or a finite value of the transverse (along $\hat{x}$) gradient of the longitudinal flow velocity. How the total angular momentum is distributed to the longitudinal flow shear and the magnitude of the local relative orbital angular momentum depend on the parton production mechanism and their longitudinal momentum distributions. We consider two different scenarios in this paper: Landau fireball and Bjorken scaling model.

By momentum conservation, the average initial collective longitudinal momentum at any given transverse position can be calculated as the total momentum difference between participating projectile and target nucleons. Since the total multiplicity in $A+A$ collisions is proportional to the number of participant nucleons [18], we can make the same assumption for the produced partons with a proportionality constant $c(s)$ at a given center-of-mass energy $\sqrt{s}$.

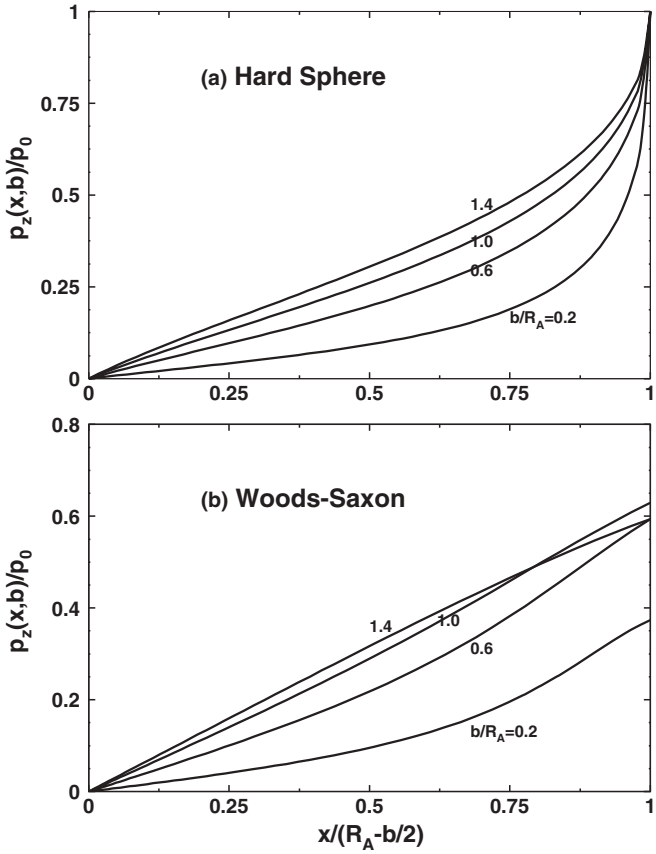

FIG. 3. Average longitudinal momentum distribution $p_z(x,b)$ in units of $p_0 = \sqrt{s}/[2c(s)]$ as a function of $x/(R_A - b/2)$ for different values of b/R_A with the hard-sphere and Woods-Saxon nuclear distributions.

In a Landau fireball model, we assume the produced partons thermalize quickly and have a common longitudinal flow velocity at a given transverse position of the overlapped region. The average collective longitudinal momentum per parton can be written as

$$p_z(x,b;\sqrt{s}) = p_0 \frac{dN^P_{\mathrm{part}}/dx - dN^T_{\mathrm{part}}/dx}{dN^P_{\mathrm{part}}/dx + dN^T_{\mathrm{part}}/dx}, \quad (9)$$

where $p_0 = \sqrt{s}/[2c(s)]$. The distribution $p_z(x,b;\sqrt{s})$ is an odd function in both x and b and therefore vanishes at $x = 0$ or $b = 0$. In Fig. 3, $p_z(x,b;\sqrt{s})$ is plotted as a function of x at different impact parameters b. We see that $p_z(x,b;\sqrt{s})$ is a monotonically increasing function of x until the edge of the overlapped region $|x \pm b/2| = R_A$ beyond which it drops to zero (gradually for Woods-Saxon geometry).

From $p_z(x,b;\sqrt{s})$ one can compute the transverse gradient of the average longitudinal collective momentum per parton dp_z/dx, which is an even function of x and vanishes at $b = 0$. One can then estimate the longitudinal momentum difference Δp_z between two neighboring partons in QGP. On average, the relative orbital angular momentum for two colliding partons separated by Δx in the transverse direction is $l_y \equiv -(\Delta x)^2 dp_z/dx$. With the hard-sphere nuclear distribution, l_y is proportional to $dp_0/dx \equiv p_0/R_A = \sqrt{s}/[2c(s)R_A]$.

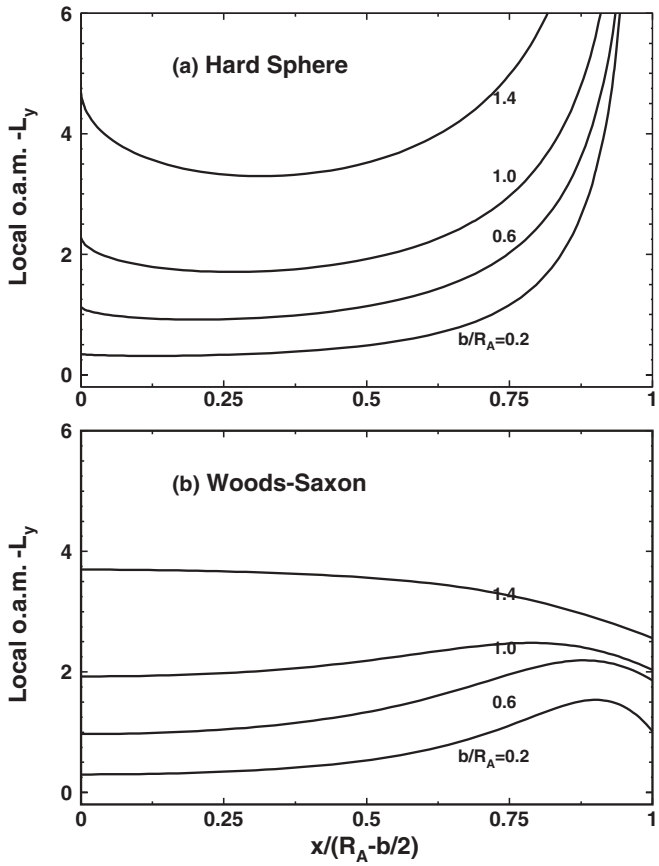

FIG. 4. Average orbital angular momentum $l_y \equiv -(\Delta x)^2 dp_z/dx$ of two neighboring partons separated by $\Delta x = 1$ fm as a function of the scaled transverse coordinate $x/(R_A - b/2)$ for different values of the impact parameter b/R_A with the hard-sphere and Woods-Saxon nuclear distributions for heavy-ion collisions at the RHIC energy with different impact parameters.

In Au+Au collisions at $\sqrt{s} = 200$ GeV, the number of charged hadrons per participating nucleon is about 15 [18]. Assuming the number of partons per (meson dominated) hadron is about 2, we have $c(s) \simeq 45$ (including neutral hadrons). Given $R_A = 6.5$ fm, $dp_0/dx \simeq 0.34$ GeV/fm, and we obtain $l_0 \equiv -(\Delta x)^2 dp_0/dx \simeq -1.7$ for $\Delta x = 1$ fm. In Fig. 4, we show the average local orbital angular momentum l_y for two neighboring partons separated by $\Delta x = 1$ fm as a function of x for different impact parameters b for both Woods-Saxon and hard-sphere nuclear distributions. We see that l_y is in general of the order of 1 and is comparable to or larger than the spin of a quark. It is expected that $c(s)$ should depend logarithmically on the colliding energy $\sqrt{s}$, therefore l_y should increase with growing $\sqrt{s}$.

In a three-dimensional expanding system, there could be a strong correlation between longitudinal flow velocity and spatial coordinate of the fluid cell. The most simplified picture is the Bjorken scaling scenario [19] in which the longitudinal flow velocity is identical to the spatial velocity $\eta = \log[(t + z)/(t - z)]$. With such correlation, local interaction and thermalization requires that a parton only interacts with other partons in the same region of longitudinal momentum or rapidity y. The width of such a region in rapidity is

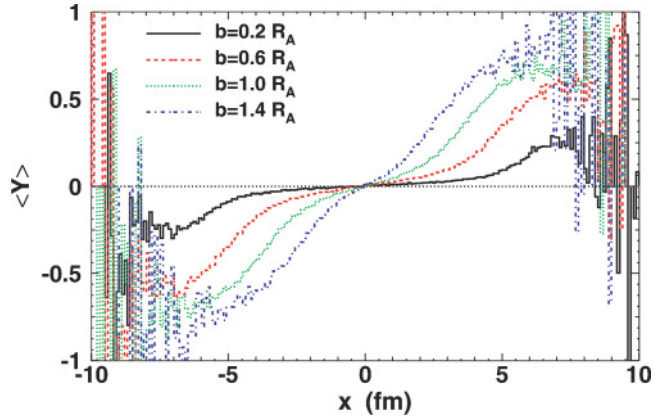

FIG. 5. (Color online) Average rapidity $\langle Y \rangle$ of the final state particles as a function of the transverse coordinate x from HIJING Mont Carlo simulations [21,22] of noncentral Au+Au collisions at $\sqrt{s} = 200$ GeV.

determined by the half-width of the thermal distribution $f(Y, p_T) = \exp[-p_T \cosh(Y - \eta)/T]$ [20], which is approximately $\Delta_Y \approx 1.5$ (with $\langle p_T \rangle \approx 2T$). The relevant measure of the local relative orbital angular momentum between two interacting partons is, therefore, the difference in parton rapidity distributions at transverse distance of $\delta x \sim 1/\mu$ on the order of the average interaction range.

One needs a dynamical model to estimate the local rapidity distributions of produced partons. For such a purpose, we use HIJING Monte Carlo model [21,22] to calculate the hadron rapidity distributions at different transverse coordinates x and assume that parton distributions of the dense matter are proportional to the final hadron spectra. Shown in Fig. 5 is the average rapidity $\langle Y \rangle$ as a function of the transverse coordinate x for different values of the impact parameter b. The distributions have exactly the same features as given by the wounded nucleon model in Fig. 3. The variation of the rapidity distributions with respect to the transverse coordinate is illustrated in Fig. 6 by the normalized rapidity

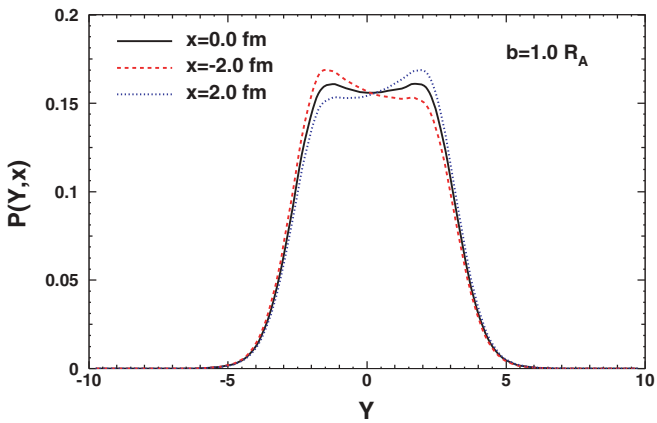

FIG. 6. (Color online) Normalized rapidity distribution of particles $P(Y, x)$ [Eq. (10)] at different transverse positions x from HIJING simulations of noncentral Au+Au collisions at $\sqrt{s} = 200$ GeV.

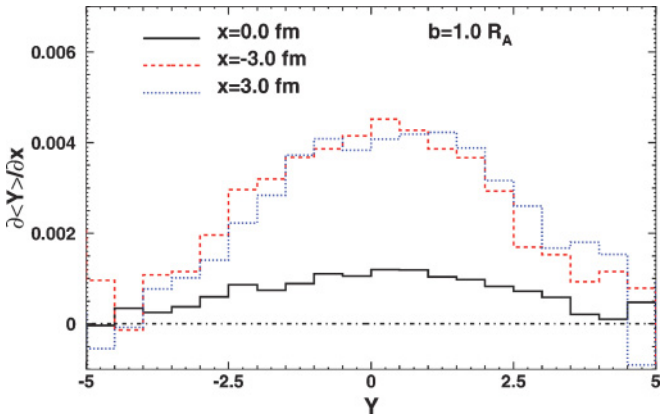

FIG. 7. (Color online) Average rapidity shear $\partial\langle Y\rangle/\partial x$ (1/fm) per unit of the transverse distance within a window $\Delta_Y = 1$ as a function of the rapidity Y at different transverse positions x from the HIJING calculation of noncentral Au+Au collisions at $\sqrt{s} = 200$ GeV.

distributions

$$P(Y,x) = \frac{dN/dx\,dY}{dN/dx} \tag{10}$$

at different transverse coordinates, $x = 0, \pm 2$ fm. At finite values of the transverse coordinates x, the normalized rapidity distributions evidently peak at larger values of rapidity $|Y|$. The shift in the shape of the rapidity distributions will provide the local longitudinal fluid shear or finite relative orbital angular momentum for two interacting partons in the local comoving frame at any given rapidity Y. To quantify such longitudinal fluid shear, one can calculate the average rapidity within an interval Δ_Y at Y,

$$\langle Y\rangle \approx Y + \frac{\Delta_Y^2}{12}\frac{1}{P(Y,x)}\frac{\partial P(Y,x)}{\partial Y}. \tag{11}$$

The average rapidity shear or the difference in average rapidity for two partons separated by a unit of transverse distance $\Delta x = 1$ fm is then,

$$\frac{\partial\langle Y\rangle}{\partial x} \approx \frac{\Delta_Y^2}{12}\frac{\partial^2 \log P(Y,x)}{\partial Y\,\partial x}. \tag{12}$$

Shown in Fig. 7 is the average rapidity shear as a function of the rapidity y at different values of the transverse coordinate x for $\Delta_Y = 1$. As we can see, the average rapidity shear has a positive and finite value in the central rapidity region. The corresponding local relative longitudinal momentum shear is

$$\frac{\partial\langle p_z\rangle}{\partial x} \approx p_T \cosh Y \frac{\partial\langle Y\rangle}{\partial x}. \tag{13}$$

With $\langle p_T\rangle \approx 2T \sim 0.8$ GeV, we have $\partial\langle p_z\rangle/\partial x \sim 0.003$ GeV/fm in the central rapidity region of a noncentral Au+Au collision at the RHIC energy given by the HIJING simulations, which is much smaller than that from a Landau fireball model estimate.

III. GLOBAL QUARK POLARIZATION

As we discussed earlier, under the longitudinal fluid shear, a pair of interacting partons will have a finite value of relative orbital angular momentum along the direction opposite to the reaction plane. In this section, we will calculate quark polarization via scatterings with fixed direction of the relative orbital angular momentum. We will assign a fixed direction of the impact parameter $\vec{x}_T$ between two interacting partons to reflect the direction of the relative orbital angular momentum. The magnitude of the relative orbital angular momentum will be characterized by the relative longitudinal momentum p between two partons separated by a transverse distance $\Delta x \sim 1/\mu$ on the order of the average interaction range. With the averaged longitudinal fluid shear dp_z/dx in the c.m. frame of the two colliding nuclei in the Landau fireball model, we have $p = \Delta x(dp_z/dx)$. In the Bjorken scaling scenario with strong correlation between spatial and momentum rapidity, the average local longitudinal shear in the comoving frame will be given by $p = \Delta x p_T \cosh(Y)\partial\langle Y\rangle/\partial x$, where p_T is the average transverse momentum.

A. Quark scattering at fixed impact parameter

We consider the scattering $q_1(P_1,\lambda_1) + q_2(P_2,\lambda_2) \to q_1(P_3,\lambda_3) + q_2(P_4,\lambda_4)$ of two quarks with different flavors, where $P_i = (E_i, \vec{p}_i)$ and λ_i in the brackets denote the four momenta and spins of the quarks, respectively. The cross section in momentum space is given by

$$d\sigma_{\lambda_3} = \frac{c_{qq}}{F}\frac{1}{4}\sum_{\lambda_1,\lambda_2,\lambda_4}\mathcal{M}(Q)\mathcal{M}^*(Q)(2\pi)^4 \times \delta(P_1+P_2-P_3-P_4)\frac{d^3\vec{p}_3}{(2\pi)^3 2E_3}\frac{d^3\vec{p}_4}{(2\pi)^3 2E_4}, \tag{14}$$

where $\mathcal{M}(Q)$ is the scattering amplitude in momentum space, $Q = P_3 - P_1 = P_2 - P_4$ is the four-momentum transfer, $c_{qq} = 2/9$ is the color factor, and $F = 4\sqrt{(P_1\cdot P_2)^2 - m_1^2 m_2^2}$ is the flux factor. Since we are interested in the polarization of one of the quarks q_1 after the scattering, we therefore average over the spins of initial quarks and sum over the spin of the quark q_2 in the final state.

We work in the c.m. frame of the two-quark system. For simplification, we neglect thermal momentum in the transverse direction and assume the relative momentum of the two quarks separated by a transverse distance Δx of the order of the effective interaction range $1/\mu$ is simply given by the longitudinal fluid shear.

One can integrate over the final momentum $\vec{p}_4$ of the quark q_2 and the longitudinal component p_{3z} of the quark q_1, and obtain

$$d\sigma_{\lambda_3} = \frac{c_{qq}}{4F}\frac{1}{4}\sum_{\lambda_1,\lambda_2,\lambda_4}\sum_{i=+,-} \times \frac{1}{E_2|p_{3z}^i| + E_1|p_{3z}^i|}\mathcal{M}(Q_i)\mathcal{M}^*(Q_i)\frac{d^2\vec{q}_T}{(2\pi)^2}, \tag{15}$$

where $p_{3z}^{\pm} = \pm\sqrt{p^2 - q_T{}^2}$, corresponding to two possible solutions of the energy-momentum conservation in the elastic scattering process, $p = |\vec{p}_1| = |\vec{p}_2|$; and $\vec{q}_T = \vec{p}_{3T}$ is the transverse momentum transfer. For simplicity, we will suppress the summation notation over $i = +, -$ hereafter, but keep in mind that the final cross section includes the two terms.

Since we would like to calculate the polarization of one final-state quark with a fixed direction of the orbital angular momentum, or fixed direction of the impact parameter, we will cast the cross section in impact parameter space by making a two-dimensional Fourier transformation in the transverse momentum transfer $\vec{q}_T$, i.e.,

$$\frac{d^2\sigma_{\lambda_3}}{d^2\vec{x}_T} = \frac{c_{qq}}{16F}\sum_{\lambda_1,\lambda_2,\lambda_4} \times \int \frac{d^2\vec{q}_T}{(2\pi)^2}\frac{d^2\vec{k}_T}{(2\pi)^2} e^{i(\vec{k}_T-\vec{q}_T)\cdot\vec{x}_T}\frac{\mathcal{M}(\vec{q}_T)}{\Lambda(\vec{q}_T)}\frac{\mathcal{M}^*(\vec{k}_T)}{\Lambda^*(\vec{k}_T)}, \quad (16)$$

where $\mathcal{M}(\vec{q}_T)$ and $\mathcal{M}(\vec{k}_T)$ are the scattering matrix elements in momentum space with four-momentum transfer $Q = (0, \vec{q})$ and $K = (0, \vec{k})$, respectively, and

$$\Lambda(\vec{q}_T) = \sqrt{(E_1 + E_2)|p_{3z}^+|}. \quad (17)$$

To calculate the quark-quark scattering amplitude in a thermal medium, we will use the hard thermal loop (HTL) resummed gluon propagator [23,25],

$$\Delta^{\mu\nu}(Q) = \frac{P_T^{\mu\nu}}{-Q^2 + \Pi_T(x)} + \frac{P_L^{\mu\nu}}{-Q^2 + \Pi_L(x)} + (\alpha - 1)\frac{Q^\mu Q^\nu}{Q^4}, \quad (18)$$

where Q denotes the gluon four-momentum and α is the gauge fixing parameter. The longitudinal and transverse projectors $P_{T,L}^{\mu\nu}$ are defined by

$$P_L^{\mu\nu} = \frac{-1}{Q^2 q^2}(\omega Q^\mu - Q^2 U^\mu)(\omega Q^\nu - Q^2 U^\nu), \quad (19)$$

$$P_T^{\mu\nu} = \tilde{g}^{\mu\nu} + \frac{\tilde{Q}^\mu \tilde{Q}^\nu}{q^2}, \quad (20)$$

with $\omega = Q\cdot U$, $\tilde{Q}_\mu = Q_\mu - U_\mu\omega$, $q^2 = -\tilde{Q}^2$, and $\tilde{g}_{\mu\nu} = g_{\mu\nu} - U_\mu U_\nu$. Here U is the fluid velocity of the local medium. The transverse and longitudinal self-energies are given by [23]

$$\Pi_L(x) = \mu_D^2\left[1 - \frac{x}{2}\ln\left(\frac{1+x}{1-x}\right) + i\frac{\pi}{2}x\right](1 - x^2), \quad (21)$$

$$\Pi_T(x) = \mu_D^2\left[\frac{x^2}{2} + \frac{x}{4}(1-x^2)\ln\left(\frac{1+x}{1-x}\right) - i\frac{\pi}{4}x(1-x^2)\right], \quad (22)$$

where $x = \omega/q$ and $\mu_D^2 = g^2(N_c + N_f/2)T^2/3$ is the Debye screening mass.

With the above HTL gluon propagator, the quark-quark scattering amplitudes can be expressed as

$$\mathcal{M}(\vec{q}_T) = \bar{u}_{\lambda_3}(P_1 + Q)\gamma_\mu u_{\lambda_1}(P_1)\Delta^{\mu\nu}(Q) \times \bar{u}_{\lambda_4}(P_2 - Q)\gamma_\nu u_{\lambda_2}(P_2), \quad (23)$$

$$\mathcal{M}^*(\vec{k}_T) = \bar{u}_{\lambda_1}(P_1)\gamma_\alpha u_{\lambda_3}(P_1 + K)\Delta^{\alpha\beta *}(K) \times \bar{u}_{\lambda_2}(P_2)\gamma_\beta u_{\lambda_4}(P_2 - K). \quad (24)$$

The product $\mathcal{M}(\vec{q}_T)\mathcal{M}^*(\vec{k}_T)$ can be converted to the following trace form,

$$\sum_{\lambda_1,\lambda_2}\mathcal{M}(\vec{q}_T)\mathcal{M}^*(\vec{k}_T) = \Delta^{\mu\nu}(Q)\Delta^{\alpha\beta *}(K)\mathrm{Tr}\big[u_{\lambda_3}(P_1 + K) \times \bar{u}_{\lambda_3}(P_1 + Q)\gamma_\mu(\not{P}_1 + m_1)\gamma_\alpha\big]\mathrm{Tr}\big[u_{\lambda_4}(P_2 - K) \times \bar{u}_{\lambda_4}(P_2 - Q)\gamma_\nu(\not{P}_2 + m_2)\gamma_\beta\big]. \quad (25)$$

In calculations of transport coefficients such as the jet energy loss parameter [24] and thermalization time [25], which generally involve cross sections weighted with transverse momentum transfer, the imaginary part of the HTL propagator in the magnetic sector is enough to regularize the infrared behavior of the transport cross sections. However, in our following calculation of quark polarization, total parton scattering cross section is involved. The contribution from the magnetic part of the interaction has therefore infrared divergence, which can only be regularized through the introduction of the nonperturbative magnetic screening mass $\mu_m \approx 0.255\sqrt{N_c/2}g^2T$ [26].

Since we have neglected the thermal momentum perpendicular to the longitudinal flow, the energy transfer $\omega = 0$ in the c.m. frame of the two colliding partons. This corresponds to setting $x = 0$ in the HTL resummed gluon propagator in Eq. (18). In this case, the c.m. frame of scattering quarks coincides with the local comoving frame of QGP, and the fluid velocity is $U^\mu = (1, 0, 0, 0)$. The corresponding HTL effective gluon propagator in Feynman gauge that contributes to the scattering amplitudes is reduced to

$$\Delta^{\mu\nu}(Q) = \frac{g^{\mu\nu} - U^\mu U^\nu}{q^2 + \mu_m^2} + \frac{U^\mu U^\nu}{q^2 + \mu_D{}^2}. \quad (26)$$

The differential cross section can in general be decomposed into a spin-independent and a spin-dependent part,

$$\frac{d^2\sigma_{\lambda_3}}{d^2\vec{x}_T} = \frac{d\sigma}{d^2\vec{x}_T} + \lambda_3\frac{d\Delta\sigma}{d^2\vec{x}_T}, \quad (27)$$

with

$$\frac{d^2\sigma}{d^2\vec{x}_T} = \frac{1}{2}\left(\frac{d\sigma_+}{d^2\vec{x}_T} + \frac{d\sigma_-}{d^2\vec{x}_T}\right), \quad (28)$$

$$\frac{d^2\Delta\sigma}{d^2\vec{x}_T} = \frac{1}{2}\left(\frac{d\sigma_+}{d^2\vec{x}_T} - \frac{d\sigma_-}{d^2\vec{x}_T}\right). \quad (29)$$

The spin-dependent part will mostly determine the polarization of the final state quark q_1 via the scattering. The calculation is involved. A simple estimate was given in Ref. [7], using a screened static potential model and small-angle approximation. In this case, the cross sections can be

written in a general form as

$$\frac{d^2\sigma}{d^2\vec{x}_T} = F(x_T, E), \tag{30}$$

$$\frac{d^2\Delta\sigma}{d^2\vec{x}_T} = \vec{n}\cdot(\vec{x}_T\times\vec{p})\Delta F(x_T, E), \tag{31}$$

where $\vec{n}$ is the polarization vector for q_1 in its rest frame. $F(x_T, E)$ and $\Delta F(x_T, E)$ are functions of both $x_T \equiv |\vec{x}_T|$ and the c.m. energy E of the two quarks. We can show that the quark-quark scattering with HTL propagators has the same form as that in the static potential model [7]. But the detailed expressions of $F(x_T, \hat{s})$ and $\Delta F(x_T, \hat{s})$ are much more complicated.

In fact, one can show that these two parts of the cross sections should have the same form as given in Eqs. (30) and (31) due to parity conservation in the scattering process. We note that in an unpolarized reaction, the cross section should be independent of any transverse direction. Hence $d\sigma/d^2\vec{x}_T$ depends only on the magnitude of x_T but not on the direction. For the spin-dependent part, the only scalar that we can construct from the available vectors is $\vec{n}\cdot(\vec{p}\times\vec{x}_T)$.

We note that, $\vec{x}_T\times\vec{p}$ is nothing but the relative orbital angular momentum of the two-quark system, $\vec{l} = \vec{x}_T\times\vec{p}$. Therefore, the polarized cross section takes its maximum when $\vec{n}$ is parallel or antiparallel to the relative orbital angular momentum, depending on whether ΔF is positive or negative. This corresponds to quark polarization in the direction $\vec{l}$ or $-\vec{l}$.

As discussed in the last section, the average relative orbital angular momentum $\vec{l}$ of two scattering quarks is in the opposite direction of the reaction plane in noncentral $A+A$ collisions. Since a given direction of $\vec{l}$ corresponds to a given direction of $\vec{x}_T$, there should be a preferred direction of $\vec{x}_T$ at a given direction of the nucleus-nucleus impact parameter $\vec{b}$. The distribution of $\vec{x}_T$ at given $\vec{b}$ depends on the collective longitudinal momentum distribution shown in the last section. For simplicity, we consider a uniform distribution of $\vec{x}_T$ in all possible directions in the upper half-xy-plane with $x > 0$. In this case, we need to integrate $d\Delta\sigma/d^2\vec{x}_T$ and $d\sigma/d^2\vec{x}_T$ over the half-plane above the y axis to obtain the average cross section at a given $\vec{b}$, i.e.,

$$\sigma = \int_0^{+\infty} dx \int_{-\infty}^{+\infty} dy \quad \frac{d^2\sigma}{d^2\vec{x}_T}, \tag{32}$$

$$\Delta\sigma = \int_0^{+\infty} dx \int_{-\infty}^{+\infty} dy \quad \frac{d^2\Delta\sigma}{d^2\vec{x}_T}. \tag{33}$$

The polarization of the quark is then obtained as

$$P_q = \frac{\Delta\sigma}{\sigma}. \tag{34}$$

B. Small angle approximation

We only consider light quarks and neglect their masses. Carrying out the traces in Eq. (25), we can obtain the expression of the cross section with HTL gluon propagators. The results are much more complicated than those obtained in Ref. [7] using a static potential model. However, if we use small-angle or small transverse momentum transfer approximation, the results are still very simple. In this case, with $q_z \sim 0$ and $q_T \equiv |\vec{q}_T| \ll p$, we obtain the spin-independent (unpolarized) cross section

$$\frac{d^2\sigma}{d^2\vec{x}_T} = \frac{g^4 c_{qq}}{8}\int \frac{d^2\vec{q}_T}{(2\pi)^2}\frac{d^2\vec{k}_T}{(2\pi)^2} e^{i(\vec{k}_T-\vec{q}_T)\cdot\vec{x}_T} \times\left(\frac{1}{q_T^2+\mu_m^2}+\frac{1}{q_T^2+\mu_D^2}\right) \times\left(\frac{1}{k_T^2+\mu_m^2}+\frac{1}{k_T^2+\mu_D^2}\right), \tag{35}$$

and the spin-dependent differential (polarized) cross section

$$\frac{d^2\Delta\sigma}{d^2\vec{x}_T} = -i\frac{g^4 c_{qq}}{16}\int \frac{d^2\vec{q}_T}{(2\pi)^2}\frac{d^2\vec{k}_T}{(2\pi)^2} e^{i(\vec{k}_T-\vec{q}_T)\cdot\vec{x}_T} \times\frac{(\vec{k}_T-\vec{q}_T)\cdot(\vec{p}\times\vec{n})}{p^2}\left(\frac{1}{q_T^2+\mu_m^2}+\frac{1}{q_T^2+\mu_D^2}\right) \times\left(\frac{1}{k_T^2+\mu_m^2}+\frac{1}{k_T^2+\mu_D^2}\right). \tag{36}$$

We note that the polarized differential cross can be related to the unpolarized one by

$$\frac{d^2\Delta\sigma}{d^2\vec{x}_T} = -\frac{1}{2p^2}(\vec{p}\times\vec{n})\cdot\vec{\nabla}_T\frac{d^2\sigma}{d^2\vec{x}_T}. \tag{37}$$

Completing the integration over the transverse momentum transfer,

$$\int\frac{d^2\vec{q}_T}{(2\pi)^2}\frac{e^{i\vec{q}_T\cdot\vec{x}_T}}{q_T^2+\mu_m^2} = \int\frac{q_T\,dq_T}{2\pi}\frac{J_0(q_T x_T)}{q_T^2+\mu_m^2}, \tag{38}$$

$$\int_0^\infty q_T\,dq_T\frac{J_0(q_T x_T)}{q_T^2+\mu_m^2} = K_0(\mu_m x_T), \tag{39}$$

where J_0 and K_0 are the Bessel and modified Bessel functions, respectively, we obtain

$$\frac{d^2\sigma}{d^2\vec{x}_T} = \frac{c_{qq}}{2}\alpha_s^2[K_0(\mu_m x_T)+K_0(\mu_D x_T)]^2, \tag{40}$$

$$\frac{d^2\Delta\sigma}{d^2\vec{x}_T} = \frac{c_{qq}\alpha_s^2}{2}\frac{(\vec{p}\times\vec{n})\cdot\hat{x}_T}{p^2}[K_0(\mu_m x_T)+K_0(\mu_D x_T)] \times[\mu_m K_1(\mu_m x_T)+\mu_D K_1(\mu_D x_T)], \tag{41}$$

where $\hat{x}_T = \vec{x}_T/x_T$ is the unit vector of $\vec{x}_T$. We compare the above results with those in the screened static potential model (SPM) where one also made the small-angle approximation,

$$\left[\frac{d\sigma}{d^2\vec{x}_T}\right]_{\rm SPM} = \frac{g^4 c_T}{4}\int\frac{d^2\vec{q}_T}{(2\pi)^2}\frac{d^2\vec{k}_T}{(2\pi)^2} e^{i(\vec{k}_T-\vec{q}_T)\cdot\vec{x}_T} \times\frac{1}{q_T^2+\mu_D^2}\frac{1}{k_T^2+\mu_D^2}, \tag{42}$$

$$\left[\frac{d\Delta\sigma}{d^2\vec{x}_T}\right]_{\rm SPM} = -i\frac{g^4 c_T}{8}\int\frac{d^2\vec{q}_T}{(2\pi)^2}\frac{d^2\vec{k}_T}{(2\pi)^2} e^{i(\vec{k}_T-\vec{q}_T)\cdot\vec{x}_T} \times\frac{(\vec{k}_T-\vec{q}_T)\cdot(\vec{p}\times\vec{n})}{p^2(q_T^2+\mu_D^2)(k_T^2+\mu_D^2)}. \tag{43}$$

We see that the only difference between the two results is the additional contributions from magnetic gluons, whose

contributions are absent in the static potential model. Using Eqs. (38) and (39), we recover the results in Ref. [7],

$$\left[\frac{d\sigma}{d^2\vec{x}_T}\right]_{\rm SPM} = \alpha_s^2 c_T K_0^2(\mu_D x_T), \tag{44}$$

$$\left[\frac{d\Delta\sigma}{d^2\vec{x}_T}\right]_{\rm SPM} = \alpha_s^2 c_T \frac{(\vec{p}\times\vec{n})\cdot\hat{\vec{x}}_T}{p^2}\mu_D K_0(\mu_D x_T)K_1(\mu_D x_T). \tag{45}$$

C. Beyond small-angle approximation

Now we present the complete results for the cross section in impact parameter space using HTL gluon propagators without the small-angle approximation. The unpolarized and polarized cross sections can be expressed in general as

$$\frac{d\sigma}{d^2\vec{x}_T} = \frac{g^4 c_{qq}}{64p^2}\int \frac{d^2\vec{q}_T}{(2\pi)^2}\frac{d^2\vec{k}_T}{(2\pi)^2}e^{i(\vec{k}_T-\vec{q}_T)\cdot\vec{x}_T}\frac{f(\vec{q}_T,\vec{k}_T)}{\Lambda(\vec{q}_T)\Lambda(\vec{k}_T)}, \tag{46}$$

$$\frac{d\Delta\sigma}{d^2\vec{x}_T} = -i\frac{g^4 c_{qq}}{64p^3}\int \frac{d^2\vec{q}_T}{(2\pi)^2}\frac{d^2\vec{k}_T}{(2\pi)^2}e^{i(\vec{k}_T-\vec{q}_T)\cdot\vec{x}_T}\frac{\Delta f(\vec{q}_T,\vec{k}_T)}{\Lambda(\vec{q}_T)\Lambda(\vec{k}_T)}, \tag{47}$$

where the kinematic factor becomes $\Lambda(\vec{q}_T)=\sqrt{2p|p_{3z}^+|}$; f and Δf are given by

$$\begin{aligned} f(\vec{q}_T,\vec{k}_T) = {} & \frac{A_{mm}(\vec{q}_T,\vec{k}_T)}{(q^2+\mu_m^2)(k^2+\mu_m^2)} \\ & + \frac{A_{ee}(\vec{q}_T,\vec{k}_T)}{(q^2+\mu_D^2)(k^2+\mu_D^2)} \\ & + \frac{A_{me}(\vec{q}_T,\vec{k}_T)}{(q^2+\mu_m^2)(k^2+\mu_D^2)} \\ & + \frac{A_{me}(\vec{k}_T,\vec{q}_T)}{(q^2+\mu_D^2)(k^2+\mu_m^2)}, \end{aligned} \tag{48}$$

$$\begin{aligned} \Delta f(\vec{q}_T,\vec{k}_T) = {} & \frac{\Delta A_{mm}(\vec{q}_T,\vec{k}_T)}{(q^2+\mu_m^2)(k^2+\mu_m^2)} \\ & + \frac{\Delta A_{ee}(\vec{q}_T,\vec{k}_T)}{(q^2+\mu_D^2)(k^2+\mu_D^2)} \\ & + \frac{\Delta A_{me}(\vec{q}_T,\vec{k}_T)}{(q^2+\mu_m^2)(k^2+\mu_D^2)} \\ & - \frac{\Delta A_{me}(\vec{k}_T,\vec{q}_T)}{(q^2+\mu_D^2)(k^2+\mu_m^2)}, \end{aligned} \tag{49}$$

$$\begin{aligned} A_{mm}(\vec{q}_T,\vec{k}_T) = {} & (\vec{q}\cdot\vec{k})^2 + 8p^2(\vec{q}\cdot\vec{k}) \\ & + 8p^3(q_z+k_z) + 16p^4, \end{aligned} \tag{50}$$

$$\begin{aligned} A_{ee}(\vec{q}_T,\vec{k}_T) = {} & A_{mm}(\vec{q}_T,\vec{k}_T) + 4p(q_z+k_z)[(\vec{q}\cdot\vec{k}) \\ & + p(q_z+k_z) + 2p^2], \end{aligned} \tag{51}$$

$$\begin{aligned} A_{me}(\vec{q}_T,\vec{k}_T) = {} & A_{mm}(\vec{q}_T,\vec{k}_T) + [-2q_z k_z(\vec{q}\cdot\vec{k}) \\ & + 4pk_z(\vec{q}\cdot\vec{k}) - 2pq_z^2 k_z \\ & - 2pq_z {k_z}^2 + 4p^2 {k_z}^2 + 8p^3 k_z)], \end{aligned} \tag{52}$$

$$\begin{aligned} \Delta A_{mm}(\vec{q}_T,\vec{k}_T) = {} & -\{[\vec{q}\cdot\vec{k} + 4p^2 - 2p(q_z+k_z)] \\ & \times (k_z\vec{q}_T - q_z\vec{k}_T) + 2p(\vec{q}\cdot\vec{k} + 4p^2)(\vec{q}_T \\ & - \vec{k}_T)\}\cdot(\vec{p}\times\vec{n}), \end{aligned} \tag{53}$$

$$\begin{aligned} \Delta A_{ee}(\vec{q}_T,\vec{k}_T) = {} & \Delta A_{mm}(\vec{q}_T,\vec{k}_T) - 4p(q_z+k_z)[(k_z\vec{q}_T \\ & - q_z\vec{k}_T) - p(\vec{k}_T - \vec{q}_T)]\cdot(\hat{p}\times\vec{n}), \end{aligned} \tag{54}$$

$$\begin{aligned} \Delta A_{me}(\vec{q}_T,\vec{k}_T) = {} & \Delta A_{mm}(\vec{q}_T,\vec{k}_T) \\ & + 2pk_z[2p(\vec{k}_T - \vec{q}_T) + (q_z - k_z)\vec{q}_T \\ & - (k_z\vec{q}_T - q_z\vec{k}_T)]\cdot(\hat{p}\times\vec{n}) + 2q_z k_z(k_z\vec{q}_T \\ & - q_z\vec{k}_T)\cdot(\hat{p}\times\vec{n}), \end{aligned} \tag{55}$$

where $p \equiv |\vec{p}|$. It is useful to note that

$$A_{mm}(\vec{q}_T,\vec{k}_T) = A_{mm}(\vec{k}_T,\vec{q}_T), \tag{56}$$

$$A_{ee}(\vec{q}_T,\vec{k}_T) = A_{ee}(\vec{k}_T,\vec{q}_T). \tag{57}$$

Hence, $f(\vec{q}_T,\vec{k}_T)$ is symmetric in its two variables

$$f(\vec{q}_T,\vec{k}_T) = f(\vec{k}_T,\vec{q}_T). \tag{58}$$

Similarly, from

$$\Delta A_{mm}(\vec{q}_T,\vec{k}_T) = -\Delta A_{mm}(\vec{k}_T,\vec{q}_T), \tag{59}$$

$$\Delta A_{ee}(\vec{q}_T,\vec{k}_T) = -\Delta A_{ee}(\vec{k}_T,\vec{q}_T), \tag{60}$$

we know that $\Delta f(\vec{q}_T,\vec{k}_T)$ is antisymmetric,

$$\Delta f(\vec{q}_T,\vec{k}_T) = -\Delta f(\vec{k}_T,\vec{q}_T). \tag{61}$$

As mentioned above, to get the average polarization for a fixed direction of the reaction plane in heavy-ion collisions, we need to average over the distribution of $\vec{x}_T$. For this purpose, we take the approach as in Ref. [7], and integrate $d\sigma/d^2\vec{x}_T$ and $d\Delta\sigma/d^2\vec{x}_T$ over the half plane above the y axis as shown in Eqs. (32) and (33). It is convenient to carry out first the integration over x and y then that over $\vec{q}_T$ and $\vec{k}_T$. To do this, we use the identity,

$$\begin{aligned} & 2\int_0^{+\infty}\frac{dx}{2\pi}\int_{-\infty}^{+\infty}\frac{dy}{2\pi}e^{i(\vec{k}_T-\vec{q}_T)\cdot\vec{x}_T} \\ & \quad = \delta^2(\vec{k}_T - \vec{q}_T) + \frac{i}{\pi}\delta(k_y - q_y)\mathcal{P}\frac{1}{k_x - q_x}, \end{aligned} \tag{62}$$

where $\mathcal{P}$ denotes the principal value.

It is useful to note that $\delta^2(\vec{k}_T - \vec{q}_T) = \delta^2(\vec{q}_T - \vec{k}_T)$ and $\mathcal{P}\frac{1}{k_x-q_x} = -\mathcal{P}\frac{1}{q_x-k_x}$. Therefore, only the first term on the right-hand side of Eq. (62) contributes to the total unpolarized cross section,

$$\sigma = \frac{g^4 c_{qq}}{64p^2}\frac{1}{2}\int_{q_T\leqslant p}\frac{d^2\vec{q}_T}{(2\pi)^2}\frac{f(\vec{q}_T,\vec{q}_T)}{\Lambda^2(\vec{q}_T)}. \tag{63}$$

The polarized cross section $\Delta\sigma$ receives a contribution only from the second term,

$$\begin{aligned} \Delta\sigma = {} & \frac{g^4 c_{qq}}{64p^3}\int_{-p}^{p}\frac{dq_y}{2\pi}\int_{-\sqrt{p^2-q_y^2}}^{\sqrt{p^2-q_y^2}}\frac{dq_x}{2\pi}\int_{-\sqrt{p^2-q_y^2}}^{\sqrt{p^2-q_y^2}}\frac{dk_x}{2\pi} \\ & \times\frac{1}{k_x - q_x}\frac{\Delta f(q_x,q_y;k_x,q_y)}{\Lambda(\vec{q}_T)\Lambda(\vec{k}_T)}. \end{aligned} \tag{64}$$

Changing the integration variable $q_T = p\sin\theta$ and $\xi = \sin^2(\theta/2)$ in the expression of the total cross section σ, we obtain

$$\sigma = \frac{\pi c_{qq}\alpha_s^2}{4\hat{s}}\int_0^1 d\xi\left\{\frac{1+\xi^2}{(\xi+\beta_m\tilde{T}^2)^2}+\frac{(1-\xi)^2}{(\xi+\beta_D\tilde{T}^2)^2} + \frac{2(1-\xi)}{(\xi+\beta_D\tilde{T}^2)(\xi+\beta_m\tilde{T}^2)}\right\}, \tag{65}$$

where $\beta_D = (\mu_D/T)^2 = 4\pi\alpha_s(N_c+N_f/2)/3$, $\beta_m = (\mu_m/T)^2 = 0.255^2(4\pi)^2\alpha_s^2 N_c/2$, and $\tilde{T} = T/\sqrt{\hat{s}}$ with $\sqrt{\hat{s}}$ the center of mass energy of the qq system. The integration can be carried out analytically,

$$\sigma = \frac{\pi c_{qq}\alpha_s^2}{4\hat{s}}\left\{4+\frac{1}{\beta_m\tilde{T}^2}+\frac{1}{\beta_D\tilde{T}^2}-\frac{2}{1+\beta_m\tilde{T}^2} - 2\left(\beta_m\tilde{T}^2+\frac{1+\beta_m\tilde{T}^2}{\beta_m\tilde{T}^2-\beta_D\tilde{T}^2}\right)\ln\left(1+\frac{1}{\beta_m\tilde{T}^2}\right) - 2\left(\beta_D\tilde{T}^2+\frac{\beta_m\tilde{T}^2-2\beta_D\tilde{T}^2-1}{\beta_m\tilde{T}^2-\beta_D\tilde{T}^2}\right)\ln\left(1+\frac{1}{\beta_D\tilde{T}^2}\right)\right\}. \tag{66}$$

Similarly, we make the variable substitutions $q_y = p\sqrt{1-t^2}$, $q_x = pt\sqrt{1-\xi^2}$, $k_x = pt\sqrt{1-\eta^2}$ in the integration for $\Delta\sigma$ and obtain

$$\begin{aligned}\Delta\sigma &= -\frac{c_{qq}\alpha_s^2}{8\pi\hat{s}}\int_{-1}^1 dt\int_0^1 d\xi\int_0^1 d\eta\frac{t^2\sqrt{\xi\eta}}{\sqrt{1-t^2}\sqrt{1-\xi^2}\sqrt{1-\eta^2}}\\ &\times\left\{\frac{(1-t^2)(4+t\xi+t\eta)-2(t^2\xi\eta+1)+2t(1+\xi\eta)(5+t^2\xi\eta)/(\xi+\eta)}{(1-t\xi+2\beta_m\tilde{T}^2)(1-t\eta+2\beta_m\tilde{T}^2)}\right.\\ &+\frac{(1-t^2)(t\xi+t\eta)+2(t^2\xi\eta+1)+2t(1+\xi\eta)(1+t^2\xi\eta)/(\xi+\eta)}{(1-t\xi+2\beta_D\tilde{T}^2)(1-t\eta+2\beta_D\tilde{T}^2)}\\ &\left.+\frac{2(1-t^2)(2+t\xi+t\eta)+8t(1+\xi\eta)(1+t\eta)/(\xi+\eta)}{(1-t\xi+2\beta_m\tilde{T}^2)(1-t\eta+2\beta_D\tilde{T}^2)}\right\}.\end{aligned} \tag{67}$$

Note that in the calculation of both the polarized and unpolarized cross sections, we have limited the range of integration over the transverse momentum due to energy conservation. Such restriction is not imposed in the small-angle approximation in Ref. [7]. We see that, at given β_m and β_D, both σ and $\Delta\sigma$ are functions of the variable $\tilde{T} = T/\sqrt{\hat{s}}$. Since β_m and β_D depend on α_s, the polarization $P_q = \Delta\sigma/\sigma$ also depends on the value of α_s.

We can now carry out the integration numerically to get the quark polarization P_q. Before we show the numerical results, it is useful to look at two limits.

(i) *High-energy limit*. At very high energies, $\sqrt{\hat{s}} \gg T$ or $\tilde{T} \ll 1$, we have

$$\sigma = \frac{\pi c_{qq}\alpha_s^2}{4\hat{s}\tilde{T}^2}\left\{\frac{1}{(1+4\beta_m\tilde{T}^2)\beta_m}+\frac{1}{(1+4\beta_D\tilde{T}^2)\beta_D} + \frac{2}{\beta_D-\beta_m}\ln\frac{\beta_D(1+4\beta_m\tilde{T}^2)}{\beta_m(1+4\beta_D\tilde{T}^2)}\right\}, \tag{68}$$

$$\Delta\sigma = -\frac{4c_{qq}\alpha_s^2}{\pi\hat{s}}\int_0^1 dt\left[\frac{1}{\sqrt{t^2+4\beta_m\tilde{T}^2}}\tan^{-1}\sqrt{\frac{1-t^2}{t^2+4\beta_m\tilde{T}^2}} + \frac{1}{\sqrt{t^2+4\beta_D\tilde{T}^2}}\tan^{-1}\sqrt{\frac{1-t^2}{t^2+4\beta_D\tilde{T}^2}}\right]^2. \tag{69}$$

This is the case where the small-angle approximation can be made. The above can also be obtained from Eqs. (35) and (36) by carrying out the integration over $\vec{x}_T$ in the half-plane of $x > 0$.

(ii) *Low-energy limit*. In the limit $\sqrt{\hat{s}} \ll T$, we have $q_T^2+\mu_D^2 \approx \mu_D^2$ and $q_T^2+\mu_m^2 \approx \mu_m^2$, the cross sections become

$$\sigma = \frac{c_{qq}\alpha_s^2}{8\hat{s}}\pi\left(\frac{\sqrt{\hat{s}}}{T}\right)^4\left(\frac{8}{3\beta_m^2}+\frac{2}{3\beta_D^2}+\frac{2}{\beta_m\beta_D}\right), \tag{70}$$

$$\begin{aligned}\Delta\sigma = -\frac{c_{qq}\alpha_s^2}{16\pi\hat{s}}\left(\frac{\sqrt{\hat{s}}}{T}\right)^4\left[-\frac{1}{\beta_m^2}\left(\frac{1}{192}\Gamma^4\left(\frac{1}{4}\right)+\frac{1}{2}\Gamma^4\left(\frac{3}{4}\right)\right)\right.\\ +\frac{1}{\beta_D^2}\left(\frac{1}{192}\Gamma^4\left(\frac{1}{4}\right)+\Gamma^4\left(\frac{3}{4}\right)\right)\\ \left.+\frac{2}{\beta_m\beta_D}\left(\frac{1}{192}\Gamma^4\left(\frac{1}{4}\right)+\Gamma^4\left(\frac{3}{4}\right)\right)\right].\end{aligned} \tag{71}$$

Given the corresponding values of the Γ function, one can obtain numerically

$$\Delta\sigma \approx -\frac{c_{qq}\alpha_s^2}{16\pi\hat{s}}\left(\frac{\sqrt{\hat{s}}}{T}\right)^4\left(-\frac{2.03}{\beta_m^2}+\frac{3.15}{\beta_D^2}+\frac{6.30}{\beta_m\beta_D}\right). \tag{72}$$

We see that in the low-energy limit, the magnetic part contributes with a different sign from the electric one. The polarization $P_q = \Delta\sigma/\sigma$ is given by

$$P_q \approx -\frac{3}{2\pi^2}\frac{-2.03\beta_D^2 + 3.15\beta_m^2 + 6.30\beta_m\beta_D}{8\beta_D^2 + 2\beta_m^2 + 6\beta_m\beta_D}, \tag{73}$$

which tends to be a constant in this low-energy limit. In the weak coupling limit $\alpha_s \ll 1$, $\beta_D \gg \beta_m$, the above constant $P_q \approx 0.04$ is a small positive number.

It is also interesting to look at the contributions from the electric part only. The corresponding cross sections, denoted with subscript E, are

$$\left(\frac{d\sigma}{d^2\vec{x}_T}\right)_E = \frac{g^4 c_{qq}}{64p^2}\int\frac{d^2\vec{q}_T}{(2\pi)^2}\frac{d^2\vec{k}_T}{(2\pi)^2} \times \frac{A_{ee}(\vec{q}_T,\vec{k}_T)e^{i(\vec{k}_T-\vec{q}_T)\cdot\vec{x}_T}}{\Lambda(\vec{q}_T)\Lambda(\vec{k}_T)(q^2+\mu_D^2)(k^2+\mu_D^2)}, \tag{74}$$

$$\left(\frac{d\Delta\sigma}{d^2\vec{x}_T}\right)_E = -i\frac{g^4 c_{qq}}{64p^3}\int\frac{d^2\vec{q}_T}{(2\pi)^2}\frac{d^2\vec{k}_T}{(2\pi)^2} \times \frac{\Delta A_{ee}(\vec{q}_T,\vec{k}_T)e^{i(\vec{k}_T-\vec{q}_T)\cdot\vec{x}_T}}{\Lambda(\vec{q}_T)\Lambda(\vec{k}_T)(q^2+\mu_D^2)(k^2+\mu_D^2)}. \tag{75}$$

Carrying out the integration over $d^2\vec{x}_T$ in the half-plane with $x > 0$, we obtain

$$\sigma_E = \frac{\pi c_{qq}\alpha_s^2}{4\hat{s}}\int_0^1\frac{(1-\xi)^2 d\xi}{(\xi+\beta_D\tilde{T}^2)^2} = \frac{\pi c_{qq}\alpha_s^2}{4\hat{s}}\left[2+\frac{1}{\beta_D\tilde{T}^2}-2(1+\beta_D\tilde{T}^2)\ln(1+\frac{1}{\beta_D\tilde{T}^2})\right], \tag{76}$$

$$\Delta\sigma_E = -\frac{c_{qq}\alpha_s^2}{8\pi\hat{s}}\int_{-1}^1 dt\int_0^1 d\xi\int_0^1 d\eta\frac{t^2\sqrt{\xi\eta}}{\sqrt{1-t^2}\sqrt{1-\xi^2}\sqrt{1-\eta^2}} \times\left\{\frac{(1-t^2)(t\xi+t\eta)+2(t^2\xi\eta+1)+2t(1+\xi\eta)(1+t^2\xi\eta)/(\xi+\eta)}{(1-t\xi+2\beta_D\tilde{T}^2)(1-t\eta+2\beta_D\tilde{T}^2)}\right\}. \tag{77}$$

In the high-energy limit, where the small-angle approximation is applicable, we have

$$\sigma_E = \frac{\pi c_{qq}\alpha_s^2}{4\hat{s}\beta_D\tilde{T}^2(1+4\beta_D\tilde{T}^2)}, \tag{78}$$

$$\Delta\sigma_E = -\frac{4c_{qq}\alpha_s^2}{\pi\hat{s}}\int_0^1\frac{dt}{t^2+4\beta_D\tilde{T}^2}\left[\tan^{-1}\sqrt{\frac{1-t^2}{t^2+4\beta_D\tilde{T}^2}}\right]^2. \tag{79}$$

In the low-energy limit, we have

$$\sigma_E = \frac{c_{qq}\alpha_s^2}{12\hat{s}\beta_D^2}\pi\left(\frac{\sqrt{\hat{s}}}{T}\right)^4, \tag{80}$$

$$\Delta\sigma_E = -\frac{c_{qq}\alpha_s^2}{16\pi\hat{s}}\left(\frac{\sqrt{\hat{s}}}{T}\right)^4\frac{1}{\beta_D^2}\left(\frac{1}{192}\Gamma^4\left(\frac{1}{4}\right)+\Gamma^4\left(\frac{3}{4}\right)\right). \tag{81}$$

The polarization in this case

$$P_q^E \equiv \frac{\Delta\sigma_E}{\sigma_E} = -\frac{3}{4\pi^2}\left(\frac{1}{192}\Gamma^4\left(\frac{1}{4}\right)+\Gamma^4\left(\frac{3}{4}\right)\right)\approx -0.24 \tag{82}$$

is a negative constant, which can also be obtained from Eq. (73) by taking the limit $\beta_m \gg \beta_D$.

D. Numerical results and comparison with data

We now carry out the integration in Eq. (67) numerically and obtain the results for the quark polarization at intermediate energies between the high- and low-energy limits. The results are shown in Fig. 8 as functions of $\sqrt{\hat{s}}/T$. The quark polarization $(-P_q)$ along the reaction plane approaches a small negative value, as we have shown in the last subsection in the low-energy limit. The value of the low-energy limit varies with α_s as given by Eq. (73). Such a dependence on α_s is a consequence of the magnetic and electric screening masses in the polarized and unpolarized cross sections which have different dependence on α_s. However, from Eq. (73), the low-energy limit of the quark polarization becomes independent of α_s in the weak coupling limit $\alpha_s \to 0$ when $\beta_m \ll \beta_D$.

As one increases the relative c.m. energy, the quark polarization changes drastically with $\sqrt{\hat{s}}/T$. It increases to some maximum value and then decreases with the growing energy, approaching the result of then small-angle approximation in the high-energy limit. This structure is caused by the interpolation between the high-energy and low-energy

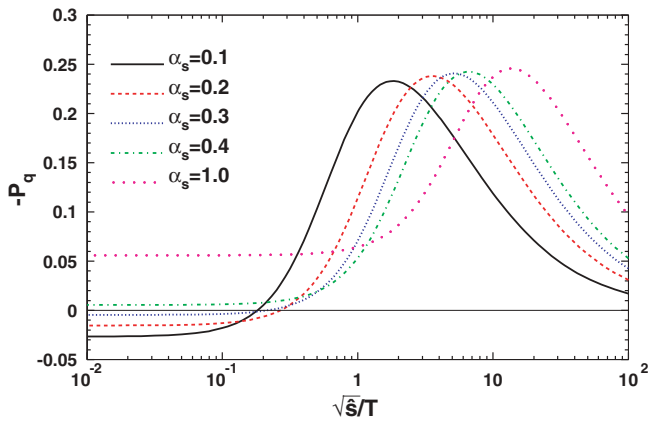

FIG. 8. (Color online) Quark polarization $-P_q$ as a function of $\sqrt{\hat{s}}/T$ for different values of α_s.

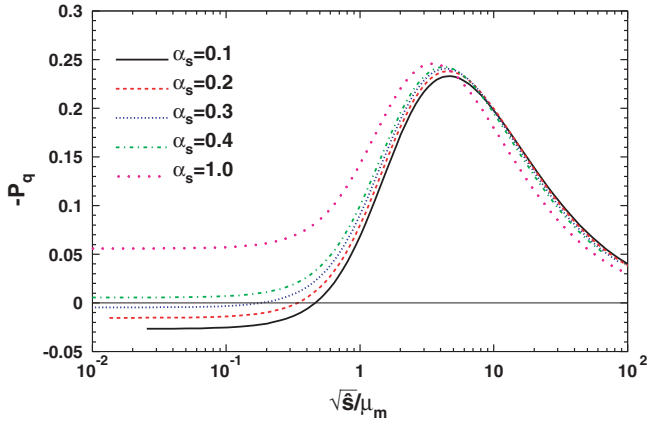

FIG. 9. (Color online) Quark polarization $-P_q$ as a function of $\sqrt{\hat{s}}/\mu_m$ for different values of α_s.

behavior dominated by the magnetic part of the interaction in the weak coupling limit $\alpha_s < 1$. Therefore, the position of the maxima in $\sqrt{\hat{s}}$ should approximately scale with the magnetic mass μ_m. This is indeed the case, as shown in Fig. 9.

To further understand the interpolation between the high- and low-energy limits in the numerical results, we also compare them in Fig. 10 with the results with the electric gluon exchange only. Without the contribution from the magnetic gluon interaction, the quark polarization takes a relatively large value $P_q \approx -0.24$ at low energies and then decreases with $\sqrt{\hat{s}}$ at high energies. The magnetic interaction in the low-energy limit apparently has a different sign in the contribution to the polarized cross section relative to that of the electric one. The net polarization is therefore reduced at finite α_s to smaller negative values when $\alpha_s \ll 1$. The electric contribution to the net quark polarization also corresponds to the limit $\mu_m \gg \mu_D$ or $\alpha_s \gg 1$ in the full result. Even though our perturbative approach is no longer valid in such a limit, it indicates that the net quark polarization remains a finite negative value in the strong coupling limit as shown in Fig. 9.

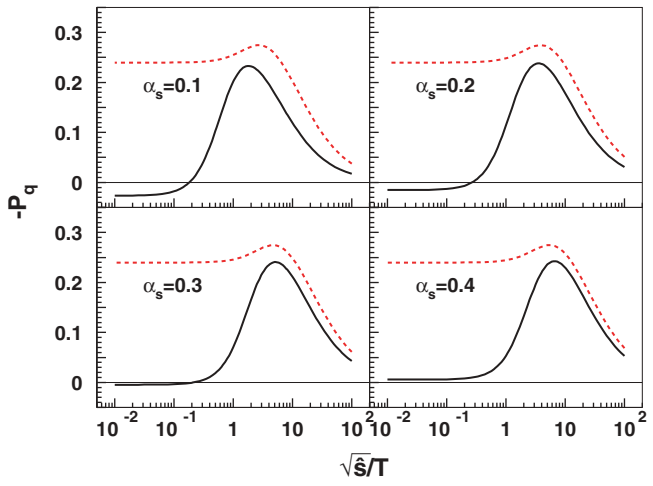

FIG. 10. (Color online) Quark polarization $-P_q$ as a function of $\sqrt{\hat{s}}/T$ with the full HTL gluon propagator (solid) compared with the results with the electric part of the interaction only (dashed).

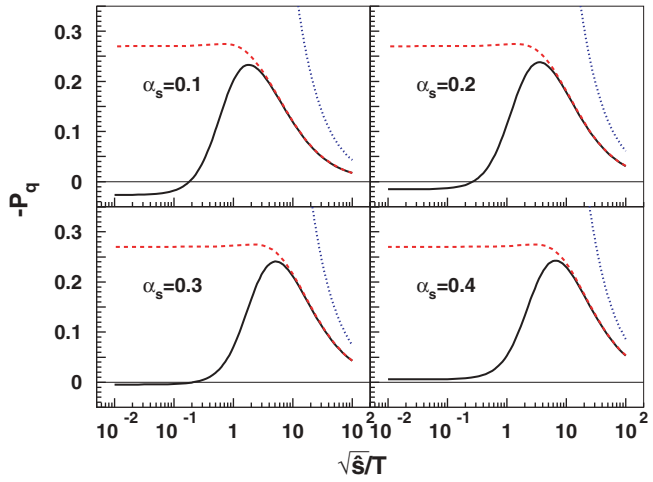

FIG. 11. (Color online) Comparison of the results obtained using HTL gluon propagator (solid line) with those under the small-angle approximation (dashed line) and those using the screened static potential model under the small-angle approximation (dotted line).

In Fig. 11 we also compare the full numerical results (solid lines) with those of the small-angle approximation in the high-energy limit (dashed lines) as given by Eqs. (68) and (69). These two groups of results indeed agree with each other at high energies. However, they both are different from the results of the static potential model in the small angle limit (dotted lines) [9] which does not have the energy conservation restriction in the integration over the transverse momentum transfer.

In semiperipheral Au+Au collisions ($b = R_A$) at the RHIC energy, one can assume an average temperature $T \approx 400$ MeV [27]. With $\alpha_s \approx 0.3$ and $\mu_m = 0.47$ GeV, the global quark polarization reaches its peak value at c.m. energy about 1.8 GeV. Since the magnetic interaction dominates the quark-quark interaction in our calculation, we can assume that the average interaction range in the transverse direction is given by the magnetic mass, $\Delta x \sim 1/\mu_m$. According to our estimates of the longitudinal fluid shear, the average c.m. energy of the quark pair under such fluid shear is $\sqrt{\hat{s}} \sim 0.08\tilde{}\text{GeV}^2/\mu_m \approx 0.17$ GeV (from Fig. 4) in the Landau fireball model. In the Bjorken scaling model (from Fig. 7), the c.m. energy provided by the local fluid shear is $\sqrt{\hat{s}} \sim 0.004\langle p_T\rangle \cosh(y)\text{fm}^{-1}/\mu_m \approx 0.001$ GeV in the central rapidity region (we assume $\langle p_T\rangle \sim 2T$). In both cases, the longitudinal fluid shear is so weak that the global quark polarization due to perturbative quark-quark scatterings is very small (close to zero) according to our numerical calculations that go beyond the small-angle approximation.

As has been pointed out in Refs. [7,9], the global quark polarization can be transferred to final hadrons and lead to global polarization of hyperons and spin alignment of vector mesons in noncentral $A+A$ collisions. The magnitudes of global hyperon polarizations depend on the hadronization mechanisms but are of the same order of P_q. For the vector meson spin alignments, the effect is independent of the direction of the reaction plane, but the magnitude can only be of the order of P_q^2. Measurements on both global hyperon

polarization and vector meson spin alignment have been carried out [10–16]. Within the large statistic errors of the current measurements, no significant global polarization was found that was consistent with our calculations presented above. However, the statistics are not high enough to make any definitive conclusions. According to our estimate in the Bjorken scaling scenario of the HIJING model, the fluid shear increases rapidly with rapidity [Eq. (13)]. It will be helpful to have measurements in the forward rapidity region where the effect of quark polarization might be large enough to be measurable.

In heavy-ion collisions at the CERN Large Hadron Collider (LHC) energy $\sqrt{s} = 5.5$ TeV, the average multiplicity density per participant nucleon pair was estimated to be about a factor of 3 larger than that at the RHIC energy [28]. The corresponding longitudinal fluid shear and the average c.m. energy of a quark pair will be about a factor 6 larger than that at the RHIC energy in the Landau fireball model, assuming the temperature is about 1.44 higher. One can also expect the average local longitudinal fluid shear in the Bjorken scenario at LHC to be similarly amplified over that at the RHIC energy, particularly at large rapidity. Therefore, the resulting net quark polarization should also be larger at LHC.

IV. CONCLUSIONS AND DISCUSSIONS

In this paper, we have extended an earlier study [9] of the global quark polarization caused by the longitudinal fluid shear in noncentral heavy-ion collisions. We have calculated the average local relative orbital angular momentum or longitudinal fluid shear with two extreme models: Landau fireball and Bjorken scaling. In the Landau fireball model, we assumed a wounded nucleon model for local particle production with both the hard-sphere and Woods-Saxon nuclear distributions. Each parton is then assumed to carry an average longitudinal flow velocity calculated from the net longitudinal momentum at a given transverse position. In the Bjorken scaling model, we considered correlation between spatial and momentum rapidity in a three-dimensional expanding system for which we calculated the average rapidity or longitudinal momentum shear (derivative of the average rapidity or the longitudinal momentum) with respect to the transverse position x. The shear determines the local relative orbital angular momentum in the comoving frame at a given rapidity. These two model calculations provide estimates of the local fluid shear in two extreme limits.

We have also extended the calculation of the global quark polarization P_q within perturbative QCD at finite temperature beyond the small-angle approximation of the previous study [9], which might not be valid for small values of the local longitudinal fluid shear or the average c.m. energy $\sqrt{\hat{s}}$ of a colliding quark pair. We found that the magnetic part of the interaction in one-gluon exchange is particularly important at low energies, which cancels the contribution from the electric interaction and leads to smaller negative values of the net quark polarization in the weak coupling limit ($\alpha_s < 1$). The final global quark polarization therefore is small in both the low- and high-energy limits. It can, however, reach a peak value of about $P_q \approx -0.24$ at an energy determined by the nonperturbative magnetic mass $\sqrt{\hat{s}} \sim 4\mu_m \approx g^2 T\sqrt{N_c/2}$. For $\sqrt{\hat{s}} < \mu_m$, the average quark polarization becomes significantly smaller.

For Au+Au collisions at RHIC, the longitudinal fluid shear in both Landau and Bjorken models is so weak that the global quark polarization due to perturbative quark-quark scatterings is quite small according to our estimates that go beyond the small-angle approximation. The effect is expected to be larger at LHC.

We want to emphasize that the numerical estimate presented above is based on a perturbative calculation via quark-quark scatterings in the weak coupling limit. It is still possible that quarks could acquire large global polarization through interaction in the strong coupling limit, as hinted at by our results with large values of the strong coupling constant even though such a perturbative approach becomes invalid. The finite value of the quark polarization could be detected via measurements of the global hyperon polarization or the vector meson spin alignment with respect to the reaction plane. According to our estimate of the longitudinal fluid shear, the effect is more significant at large rapidity under the Bjorken scenario of the initial parton production. The effect could be also larger in the case of jet production, where fluid shear is apparently much more significant [8].

In the limit of vanishing local orbital angular momentum provided by the longitudinal fluid shear, the approach we used in this paper in the impact-parameter representation might not be valid anymore. However, the final spin-polarization due to the spin-orbital interaction should approach zero in this limit, which is approximately the result of our full calculation.

ACKNOWLEDGMENTS

The authors thank B. Muller for pointing out the scenario of Bjorken scaling model of initial parton production and J. Deng for his help in the numerical calculation of the local orbital angular momentum with the Woods-Saxon geometry. This work was supported in part by National Natural Science Foundation of China (NSFC) under Grant No. 10525523, the startup grant from the University of Science and Technology of China (USTC) in association with the "100 Talents" project of Chinese Academy of Sciences (CAS), the NSFC Grant No. 10675109, and the U.S. Department of Energy under Contract No. DE-AC03-76SF00098.

[1] M. Gyulassy and L. McLerran, Nucl. Phys. **A750**, 30 (2005).
[2] P. Jacobs and X. N. Wang, Prog. Part. Nucl. Phys. **54**, 443 (2005).
[3] K. H. Ackermann *et al.* (STAR Collaboration), Phys. Rev. Lett. **86**, 402 (2001).
[4] D. Teaney, Phys. Rev. C **68**, 034913 (2003).
[5] A. Majumder, B. Muller, and X. N. Wang, Phys. Rev. Lett. **99**, 192301 (2007).
[6] A. Adil and M. Gyulassy, Phys. Rev. C **72**, 034907 (2005); A. Adil, M. Gyulassy, and T. Hirano, Phys. Rev. D **73**, 074006 (2006).

[7] Z. T. Liang and X. N. Wang, Phys. Rev. Lett. **94**, 102301 (2005); Erratum-*ibid*. **96**, 039901 (2006).
[8] B. Betz, M. Gyulassy, and G. Torrieri, Phys. Rev. C **76**, 044901 (2007).
[9] Z. T. Liang and X. N. Wang, Phys. Lett. **B629**, 20 (2005).
[10] I. Selyuzhenkov (STAR Collaboration), AIP Conf. Proc. **870**, 712 (2006).
[11] I. Selyuzhenkov (STAR Collaboration), J. Phys. G: Nucl. Part. Phys. **32**, S557 (2006) [arXiv:nucl-ex/0605035].
[12] I. Selyuzhenkov (STAR Collaboration), J. Phys. G **34**, S1099 (2007).
[13] J. H. Chen (STAR Collaboration), J. Phys. G **34**, S331 (2007).
[14] I. Selyuzhenkov (STAR Collaboration), High Ener. Phys. and Nucl. Phys. **31**, 1185 (2007).
[15] Z. B. Tang (STAR Collaboration), High Ener. Phys. and Nucl. Phys. **31**, 1192 (2007).
[16] B. I. Abelev *et al*. (STAR Collaboration), Phys. Rev. C **76**, 024915 (2007).
[17] B. Cederwall *et al*., Phys. Rev. Lett. **72**, 3150 (1994).
[18] B. B. Back *et al*. (PHOBOS Collaboration), arXiv:nucl-ex/0301017; R. Nouicer *et al*. (PHOBOS Collaboration), J. Phys. G **30**, S1133 (2004).
[19] J. D. Bjorken, Phys. Rev. D **27**, 140 (1983).
[20] P. Levai, B. Muller, and X. N. Wang, Phys. Rev. C **51**, 3326 (1995).
[21] X. N. Wang and M. Gyulassy, Phys. Rev. D **44**, 3501 (1991).
[22] X. N. Wang, Phys. Rep. **280**, 287 (1997).
[23] H. A. Weldon, Phys. Rev. D **26**, 1394 (1982).
[24] X.-N. Wang, Phys. Lett. **B485**, 157 (2000).
[25] H. Heiselberg and X.-N. Wang, Nucl. Phys. **B462**, 389 (1996).
[26] T. S. Biró and B. Müller, Nucl. Phys. **A561**, 477 (1993).
[27] B. Muller and K. Rajagopal, Eur. Phys. J. C **43**, 15 (2005).
[28] S. Y. Li and X. N. Wang, Phys. Lett. **B527**, 85 (2002).